Letter

Low-Cost Synthesis of Silicon Quantum Dots with Near-Unity Internal Quantum Efficiency

Jingjian Zhou, Jing Huang, Huai Chen, Archana Samanta, Jan Linnros, Zhenyu Yang, and Ilya Sychugov*

Read Online

ACCESS | Metrics & More | Article Recommendations | Supporting Information

ABSTRACT: As a cost-effective batch synthesis method, Si quantum dots (QDs) with near-infrared photoluminescence, high quantum yield (>50% in polymer nanocomposite), and near-unity internal quantum efficiency were fabricated from an inexpensive commercial precursor (triethoxysilane, TES), using optimized annealing and etching processes. The optical properties of such QDs are similar to those prepared from state-of-the-art precursors (hydrogen silsesquioxane, HSQ) yet featuring an order of magnitude lower cost. To understand the effect of synthesis parameters on QD optical properties, we conducted a thorough comparison study between common solid precursors: TES, HSQ, and silicon monoxide (SiO), including chemical, structural, and optical characterizations. We found that the structural nonuniformity and abundance of oxide inherent to SiO limited the resultant QD performance, while for TES-derived QDs this drawback can be avoided. The presented low-cost synthetic approach would significantly favor applications requiring high loading of good-quality Si QDs, such as light conversion for photovoltaics.
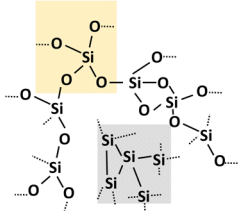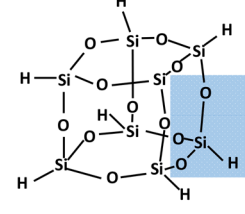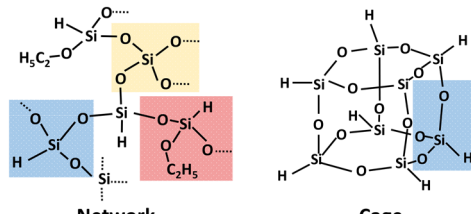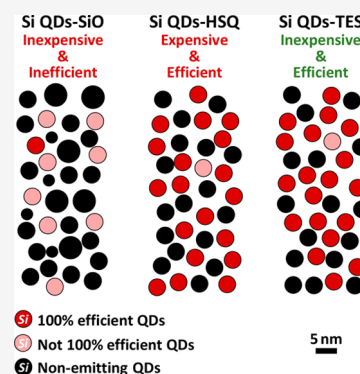
Owing to natural element abundance, nontoxicity, and unique optoelectronic properties, silicon quantum dots (Si QDs) have emerged as an attractive class of QDs, especially in the applications of biolabeling,[1−3] quantum-dot-based light-emitting diodes (QLEDs),[4,5] and semitransparent photovoltaics (PVs).[6,7] Benefiting from wavelength-tunable photoluminescence (PL),[8−10] high photoluminescence quantum yield (PLQY),[11] and a significant Stokes shift,[12] Si QDs are considered as promising fluorophores in LEDs[13,14] and luminescent solar concentrators (LSCs).[15,16] For example, Si QD-based LEDs have achieved a record external quantum efficiency (EQE) of 6.2%,[4] and an optical power efficiency of 7.9% was obtained for an LSC prototype (9 × 9 cm²) based on Si QDs/polymer nanocomposites.[6] Nevertheless, large quantities of Si QDs with a high PLQY of core-related luminescence are essential for the practical application of these technologies. Therefore, a low-cost synthesis approach of Si QDs with good quality is highly demanded.

Various methods have been developed for the synthesis of colloidal Si QDs, including top-down approaches, such as electrochemical Si wafer etching[17,18] and laser ablation of solid Si;[19] bottom-up approaches, such as reduction reaction of halosilanes;[20] and precursor decomposition and reassembly approaches, such as plasma synthesis from silane gas[21,22] and thermal pyrolysis of silicon-rich oxide compounds.[23−27] However, very few methods are suitable for the scalable production of Si QDs with a decent PLQY. One of them is a thermal pyrolysis of silicon oxide materials with a Si excess, such as hydrogen silsesquioxane (HSQ).[27] This is a highly pure material with a well-defined cage structure, which translates, however, to a costly synthesis. This HSQ-based

method is widely used to prepare ligand-passivated Si QDs with emission spanning from the visible to the near-infrared regime (700−1050 nm)[10] and a high PLQY (up to 60%, depending on the emission wavelength).[28,29] With this approach, a hybrid nanocomposite (up to ∼65% PLQY at 800 nm) comprising Si QDs and an off-stoichiometric thiol-ene (OSTE) polymer host matrix was reported for applications requiring high-quality Si QDs in a solid phase.[11] However, the high cost of HSQ hinders the mass production of Si QDs in practice.

Other starting materials with a less-defined structure and composition, hence a lower cost, have also been investigated. For example, the preparation of Si QDs using thermal-induced disproportionation of silicon monoxide (SiO) was developed.[30,31] Unfortunately, the PLQY of the Si QD ensemble (PL peak at 835 nm) was relatively low (≤15%), insufficient for light-conversion applications (at least PLQY ≥ 50% is typically required). Recently, a sol−gel polymerization reaction from inexpensive starting materials, such as HSiCl₃, trimethoxysilane (TMS), and triethoxysilane (TES), has emerged as another low-cost alternative to the expensive HSQ.[25,32,33] Here, unlike for HSQ, the resulting $HSiO_{1.5}$ polymers contain impurities, such as carbon. For instance, colloidally stable,

SiO	HSQ	TES	
Silicon Monoxide	**Hydrogen Silsesquioxane**	**Triethoxysilane**	
$SiO_n (1 < n < 2)$	$[HSiO_{1.5}]_n (n = 8)$	$HSi(OC_2H_5)_3$	
Si clusters in amorphous SiO_2 matrix	**Well-defined cage structure**	**TES-derived Xerogels consist of networks and cages**	
		Network	Cage
Annealed at 920°C for 1h	**Annealed at 1200°C for 1h**	**Annealed at 600°C for 1h and 950°C for 1h**	

Figure 1. Three types of silicious precursors for the synthesis of Si QDs, their chemical formulas, and illustrations of their molecular structures. For TES, there are a series of pretreatments to form xerogels for the subsequent annealing.
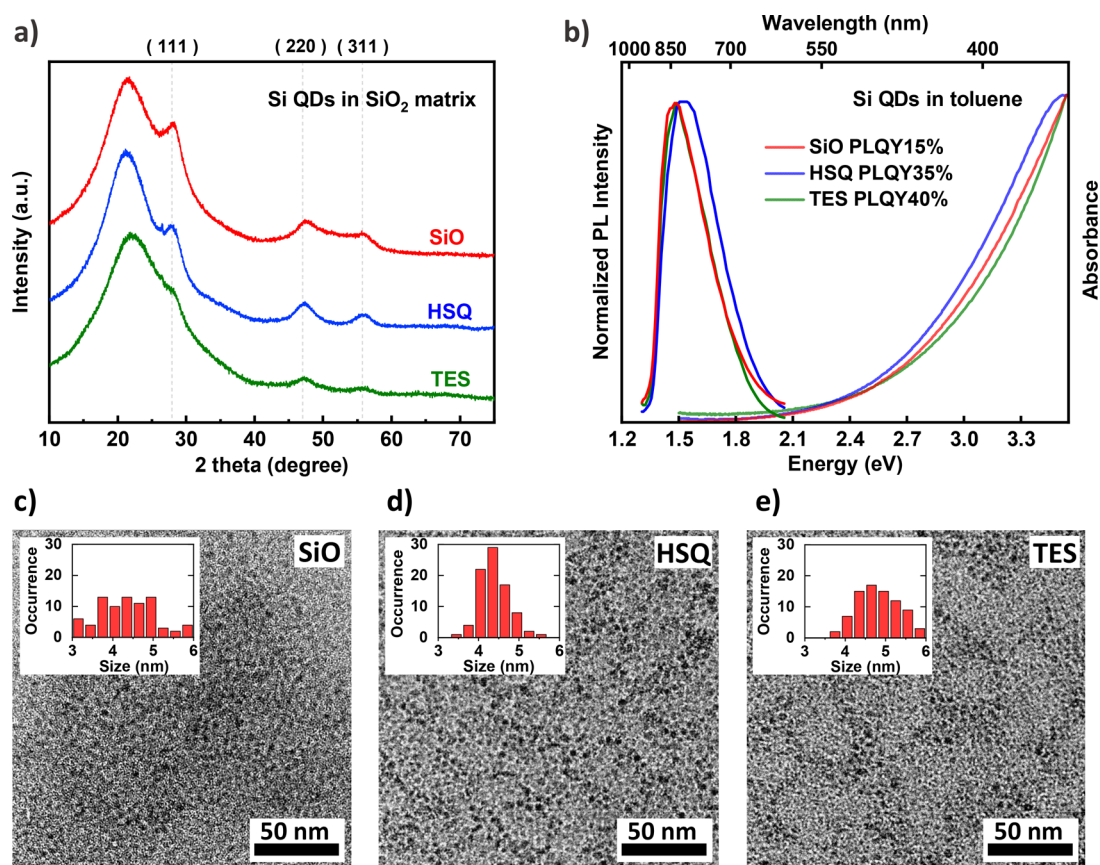
Figure 2. Chemical, optical, and structural characterizations of Si QDs synthesized from three precursors. (a) X-ray powder diffraction (XRD) spectra of the annealed HSQ (1200 °C), annealed TES-derived xerogels (950 °C), annealed SiO (920 °C). (b) Emission and absorption spectra of Si QDs in toluene synthesized from three precursors. (c−e) Transmission electron microscope (TEM) images of these Si QDs. The inset of each TEM image is the size distribution of QDs.

alkyl-capped Si QDs (PLQY ≤ 25% at 955 nm peak emission) were obtained from the reductive thermolysis of $(HSiO_{1.5})_n$ sol−gel glasses.[2,34] Saitow et al. reported a scalable and cost-effective method starting from $HSiCl_3$ relying on thermal treatment of xerogels from TMS. The TMS-derived HSQ polymer, indeed, is an inexpensive source with 380 times lower cost than HSQ. However, the PLQY of TMS-derived Si QDs was limited up to 25% (PL peak position at 800 nm), and the

mass yield difference of the final product was not accounted for.[33] Shirahata et al. applied ligand-passivated Si QDs synthesized from TES (PLQY ≤ 30%) to white LEDs[13] and deep issue imaging.[35] However, this recipe highly relies on size-selected purifications, which is unrealistic for mass production. Although extensive efforts were invested in this aspect,[25,36−39] still no emission with a high PLQY from such Si QDs has been reported. Consequently, as of now, there is no

real cost-effective synthesis method available for large-scale production of good-quality Si QDs with core-related luminescence. This limitation will significantly obstruct the development of promising technologies based on Si QDs.

Here, we present an optimized synthesis for Si QDs, based on a sol−gel polymer starting from an inexpensive TES. As a cost-effective synthesis approach, Si QDs with a near-infrared PL (∼850 nm peak), a high PLQY of ∼55% in OSTE (∼40% in toluene), and near-unity internal quantum efficiency (IQE) were fabricated (referred to as QDs-TES). We report our findings as a comparison study between HSQ (QDs-HSQ)- and SiO (QDs-SiO)-derived nanoparticles with a similar PL peak position and an identical ligand passivation. Thorough structural, chemical, and optical characterizations were performed to understand the similarities and differences between these nanomaterials. Results indicate that the intrinsic nonuniformity and the oxide phase excess prevent fabrication of good-quality QDs from SiO. TES-derived QDs, however, can be controlled sufficiently to replace HSQ as a standard starting material for Si QD synthesis.

In Figure 1, the molecular formula and structures of three silicon-rich precursors used here, HSQ, SiO, and TES, are illustrated. Corresponding annealing conditions are also provided (see detailed descriptions of optimized experimental conditions in section S1, Supporting Information). As the most commonly used precursor for the batch synthesis of Si QDs, HSQ has been comprehensively studied.[27] The constitutional unit of this well-defined molecular precursor, $[HSiO_{1.5}]_n$ ($n = 8$), is a cage-like structure with Si−O−Si frameworks and tetrahedral Si vertices. During the thermal process, the pyrolysis of Si−H groups of HSQ generates silane molecules, which diffuse throughout the surrounding matrix and decompose to form Si clusters.[26] Through crystallization at a high temperature, Si QDs are formed in an SiO_2 matrix. As for TES molecules, specific pretreatments, including hydrolysis and condensation, are required to transform them into sol−gel polymer and then dried them into xerogels for subsequent thermal annealing. The TES-derived xerogel, which is carbon-containing (unlike HSQ), is another kind of silsesquioxane with a formula $[RSiO_{1.5}]_n$ (R is either an ethoxy group or a hydrogen atom). The structure of these TES-derived xerogels is a mixture of cages and cross-linked networks.[33,40] The formation of Si QDs during annealing is similar to HSQ, except that the ethoxy groups in the TES-derived xerogels can reduce the energetic barrier for diffusion of Si atoms throughout the oxide network at the stage of Si crystallization.[25] As a result, compared to HSQ, a lower annealing temperature is required for these TES-derived xerogels, as shown in Figure 1. However, the presence of carbon may lead to undesirable impurities in the final material. As for SiO, it consists of silicon clusters and an amorphous SiO_n ($1 < n < 2$) matrix.[41] The intrinsic instability of the monoxide phase prone to complete oxidation and inherent material nonuniformity make it difficult to define its structure succinctly.

In all these samples, the high-temperature annealing leads to the formation of a nanocrystalline silicon phase. To demonstrate this fact, we carried out XRD measurements of three preannealed powders as a reference (Supporting Informaton, section S2, Figure S1) and the annealed HSQ (blue), TES-derived xerogels (green), and SiO (red) powders (Figure 2a). The broad signals centered at 21° in the reference XRD patterns are attributed to amorphous silicon dioxide.[42] For preannealed SiO powders, the additional humps centered

at 28°, 50° are ascribed to the broadenings of the (111) (220) (311) diffraction of Si nanoclusters.[43] The characteristic peaks of Si nanocrystals located at 28°, 48°, and 55° are evident in all three annealed powders, whereas they are absent from all reference samples. This confirms that Si QDs are formed through thermal annealing. It is important to note that the intensity difference in the crystalline Si signals is attributed to the various mass percentages of Si QDs in the annealed samples, which will be further discussed later.

The absorption and PL emission spectra of Si QDs from three precursors (Figure 2b) reveal that they have almost the same absorption edge onset and PL emission peak position. In general, two distinct PL bands, the "S-band" and the "F-band", are known for Si QDs with entirely different mechanisms of emission.[44] The "S-band", with yellow to near-infrared PL and a slow microsecond lifetime, corresponds to the core-related PL from the quasidirect-bandgap transitions of Si QDs and can be tuned by the quantum confinement effect. In contrast, the "F-band", with a blue to yellow range and a fast nanosecond PL lifetime, likely originates from the surface carbon-based groups or chromophores. Here, we focus on QDs solely with the "S-band", having a significant Stokes shift, which is suitable for light-converting applications due to low reabsorption. Although the emission and absorption characteristics of all three types of Si QDs studied here are identical, their corresponding PLQY values differ. With a similar size of the QDs and the same ligand (methyl 10-undecenoate) for surface passivation, the PLQY of the ensemble QDs-TES in toluene is ∼40%, similar to that of QDs-HSQ (∼35%). However, the PLQY of the ensemble QDs-SiO is only ∼15% even after recipe optimization (Supporting Information, section S3, Table S1), close to previous record values.[45]

According to previous reports,[10,46] the ∼850 nm center wavelength corresponds to a Si QD size of 4−5 nm. This is consistent with the size of QDs measured from TEM, as shown in Figure 2c−e. The inset of each TEM image depicts the size distribution of QDs. Indeed, the mean size of Si QDs synthesized from all three precursors was 4−5 nm. However, QDs-SiO were not as uniform as the other two. From another low-magnification TEM image of the QDs-SiO sample (Figure S2), larger agglomerates are evident. The nonuniformity of QDs-SiO possibly reflects the nonuniformity of SiO, where widely distributed Si clusters serve as crystallization centers during thermal annealing. In contrast, the size distributions of QDs-HSQ and QDs-TES are nearly monodispersed.

Although TES has been used as the precursor for Si QDs synthesis previously, the resulting Si QDs always exhibited emission with a low PLQY, unsuitable for mass production of high-quality Si QDs. In this work, we successfully modified the synthesis procedures, mainly at the annealing and etching steps, and the PLQY of as-synthesized colloidal QDs was successfully enhanced.

First, the effect of annealing temperature on the peak position of the PL emission of QDs-TES was carefully investigated. The TGA curve of the TES-derived xerogels (Figure S3, green) revealed that from 220 to 450 °C the incomplete hydrolysis (residual TES) and incomplete condensation (residual silanol) product were eliminated at this stage.[47] Therefore, the TES-derived xerogels were first preannealed at 600 °C (T_1) for 1 h (t_1) to eliminate residual carbon and byproducts in the polymer, as illustrated by the inset in Figure 3, upgrading the main product purity for the subsequent high-temperature annealing. ATR results (Figure
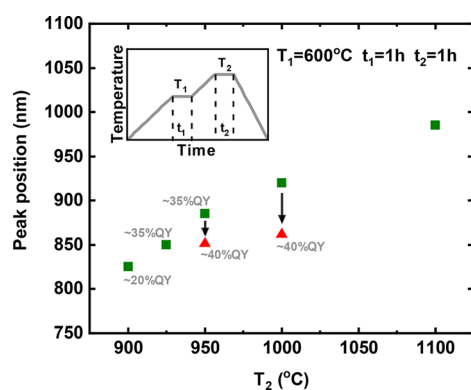
Figure 3. Effect of high annealing temperature on the peak position of the PL emission of Si QDs synthesized from TES (green squares). After HF etching was extended, the peak position can be tuned to the range of ~850 nm (red triangles). The inset illustrates the two-stage annealing process of TES-derived xerogels. Note that for Si QDs with a peak wavelength exceeding 900 nm, the PLQY values were not shown due to the limitation of detector sensitivity.

S4) show that the aging and drying process can effectively remove excess ethanol and water in the TES xerogels, while annealing at 600 °C for 1 h possibly contributes to further eliminating the byproducts from the incomplete hydrolysis and condensation that were trapped inside the polymer network, as indicated by Figure S3 and Table S2. As indicated in Figure 3, the PL peak position moved to a longer wavelength with a higher annealing temperature at the second step (T_2). Generally, higher temperatures favor the formation of larger particles, which results in red-shifted emission according to the quantum confinement effect.

Next, HF etching was also recognized as an important step for the final size of QDs-TES. On the one hand, an efficient HF etching process can etch off all the SiO_2 matrix and liberate all the Si QDs. On the other hand, excess HF (effect of amount of HF used shown in Table S3) can continuously consume surface atoms of Si QDs and make the size of QDs smaller. This is because the etching process was performed in an ambient environment, and it is inevitable that surface atoms of Si QDs would be slowly oxidized by the oxygen in the system and then be removed by the reaction with the excess HF (effect of etching time on PL peak position shown in Table S4). Therefore, to access the as-annealed size of Si QDs (shown as green squares in Figure 3), mild etching conditions (detailed in Table S5) were chosen to liberate free-standing Si QDs from the oxide matrix, minimizing the impact of HF etching on the dimension of Si QD. With extended HF etching (detailed in Table S6), the PL peak position of Si QDs annealed from a higher temperature can be also tailored to the target emission wavelength (shown as red triangles in Figure 3), although the mass yield of Si QDs becomes slightly lower inevitably (the effect of the etching time on the QD mass yield is explicitly shown in Table S7). By comparing the ensemble PLQY of Si QDs in toluene solutions, the optimal annealing condition is 950 °C annealing for 1 h with 1 h HF etching.

We attribute the benefits behind this optimal condition to a good balance of the annealing and etching processes. Under an elevated annealing temperature, the crystallinity of silicon increased, representing a well-ordered, defect-free crystalline silicon core. The extended etching process tailored the size of QDs to the target and simultaneously provided sufficient elimination of oxide around Si QDs, resulting in a PLQY

increase. For example, from the third green square (center wavelength ~885 nm) to the first red triangle (center wavelength ~850 nm) in Figure 3, it is most likely that both the size modification and the sufficient elimination of surface oxide contribute to the increase of PLQY. A "volcano-shaped" behavior of the size-dependence PLQY of Si QDs was reported in previous studies, revealing that the optimum is located at 820−830 nm.[45] The extended etching has tuned the PL center wavelength closer to the suggested optimum. The effect of the oxide amount at the QD surface on the PLQY is discussed later. As a result, this optimized recipe can be considered as a good balance of annealing and etching with an acceptable loss of mass yield of Si QDs. When annealed at 1000 °C with subsequent etching for 2 h, the PLQY of Si QDs would not further increase, and the mass yield of Si QDs becomes unacceptably low (shown in Table S7). As for the annealing time at T_2 (t_2), Table S8 indicates that the extended t_2 would favor formation of larger particles but not as effective as elevating the annealing temperature.

Similar optimization was attempted for the synthesis of QDs-SiO (shown in Table S1). However, the PLQY of QDs-SiO in toluene never exceeded 15%. Synthesis of QDs-HSQ followed an already optimized procedure.[6]

Next, solid-phase nanocomposites were fabricated, which is more relevant for applications of Si QDs in devices, such as LSCs. Si QDs were encapsulated in an off-stoichiometric thiol-ene (OSTE) polymer host matrix (experimental details in Supporting Information), which is recognized as an efficient host matrix for Si QDs.[11,48] After being embedded in OSTE, all samples showed an improved PLQY, enhanced by approximately 10−15 additional percent. The resulting PLQY of ~55% for QDs-TES in OSTE is comparable with state-of-the-art QDs-HSQ.

Table 1 shows a comparison of the cost of precursors, the QD mass yield, the relative price of QDs, and their efficiencies. With a similar high quality of QDs: ~50% PLQY in OSTE (~40% PLQY in toluene), the cost of QDs-TES is approximately 10 times lower than that of QDs-HSQ. This is an important practical result of this work. For example, a

Table 1. Price of Commercial Precursors, QD Mass Yield from Precursors, the Resulting Relative Price of Si QDs and Their Efficiencies

precursor	price USD/g	QD mass yield from precursor[a]	QD relative price[b]	PLQY
SiO	3.5−7	~6%	0.15−0.3	25 ± 3% in OSTE
				15 ± 2% in toluene
HSQ	300−360	~10%	7−15	50 ± 5% in OSTE
				35 ± 4% in toluene
TES	2.5−5	~1%	1	55 ± 6% in OSTE
				40 ± 4% in toluene

[a]Note that to estimate mass yields, the mass of Si QDs was evaluated from optical properties (absorption, QY, and emission). [b]The relative price of Si QD was calculated based on precursor quotes from different vendors, measured mass losses from annealing, and estimated mass yield of QDs. The price of "QD-TES" was set as "1". An example of mass yield estimation is given in section S4, Supporting Information.

luminescent solar concentrator (30 × 30 cm²) with ~100 mg loading of Si QDs would require ~330 USD using HSQ as the precursor, while only ~35 USD for commercial TES as the precursor following the recipe introduced here. With regard to QDs-SiO, they are not optically efficient enough for such large-scale practical applications, even though being of very low cost. Indeed, the power conversion efficiency of an LSC is proportional to the PLQY of QDs for small area devices and is even more sensitive to this parameter for large area ones.[49]

Finally, the reproducibility of the QD-TES recipe was verified by several batches of synthesis (Supporting Information, section S5, Table S9). The stability of the PLQY of QDs-TES/OSTE nanocomposite over months-long storage in ambient was also confirmed (Figure S5), which is in line with previous reports for OSTE as a stable matrix for QDs.[11,48] The dependency of the PLQY of QDs-TES/OSTE nanocomposite on the excitation wavelength is presented in Figure S6, showing a uniform response from 400 to 520 nm.

To better understand the differences and similarities in the photophysical properties of these Si QDs, we first performed spectrally resolved PL decay characterization (experimental details in Supporting Information, section S1). An example measured at 878 nm is shown in Figure 4, exhibiting a lifetime
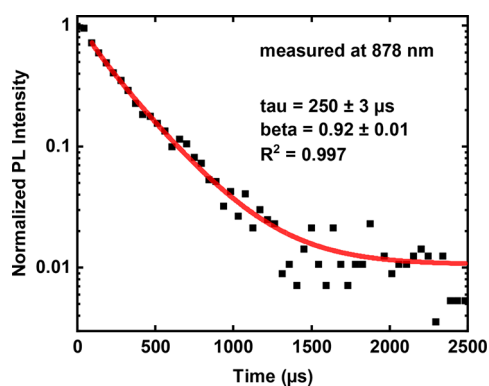

Figure 4. A spectrally resolved PL decay of QDs-TES detected at 878 nm and stretched exponential fit. The decays of QDs-SiO and QDs-HSQ detected at the same wavelength are shown in Figure S7.

of ~250 μs and a dispersion factor "beta" of 0.92 of the stretched exponential fit. A long microsecond lifetime is a typical sign of core-related PL from Si QDs, corresponding to quantum-confined radiative transitions.

A set of measurements was taken at different detection wavelengths to obtain size-dependent recombination rates. Spectrally resolved decays exclude inhomogeneous broadening in an ensemble by detecting only a narrow spectral interval (~6 nm here). However, because Si QDs have a broad homogeneous line width (~60 nm at room temperature[50]), a separate procedure is required to exclude this contribution and obtain an intrinsic recombination rate. We therefore used a "numerical size-selection" method developed here[51] and later adopted by others.[52,53] After this deconvolution procedure, we obtained nearly monoexponential spectrally resolved decays and, therefore, found intrinsic size-dependent lifetimes in a Si QD ensemble. The total recombination rate is defined as the inverse of the intrinsic lifetime. The lower the total recombination rate is, the less the nonradiative recombination is involved in the electron−hole recombination.

With known recombination rates, one can evaluate the internal quantum efficiency by comparing with a 100% IQE reference sample. In general, the ensemble PLQY, also referred to as the external quantum efficiency, characterizes the overall optical quality of the sample. It includes contributions from "bright" QDs (100% efficient), "dark" QDs (nonemitting), and "grey" QDs (not 100% efficient in the emitting state). Unlike PLQY, the IQE characterizes the efficiency of only "bright" and "grey" QDs. If "grey" QDs dominate the ensemble, the IQE is less than unity, and the nonradiative processes will limit the resulting PLQY in such QDs.

The obtained curves of the total recombination rates as a function of emission energies are plotted for each sample in Figure 5a. The total recombination rate has a clear dependence of the emission energy for all the curves, following the quantum confinement model. The values in the range near the peak emission energy (~1.45 eV) of QDs-HSQ and QDs-TES in toluene coincide well with the reference sample of a near-unity IQE,[51] indicating that there are almost no "grey" QDs in these samples. In contrast, the IQE of QDs-SiO deviates from the reference curve, suggesting the presence of additional nonradiative decay pathways.
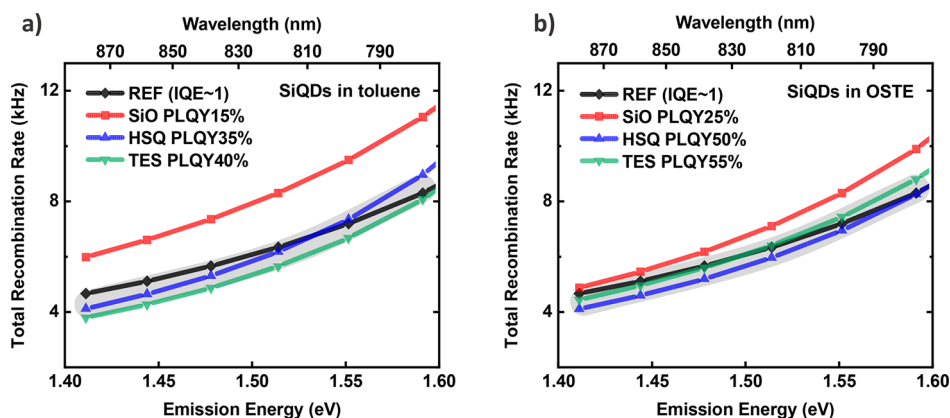
Figure 5. Total recombination rates of Si QDs synthesized from HSQ, SiO, and TES in toluene solution (a) and OSTE matrix (b). The error bar is inside the dot. Note that the reference sample was claimed to have a near-unity internal quantum efficiency in a previous paper. The gray bands at the background indicate that curves included inside have similar values and trends within experimental and analysis errors, revealing their near-unity IQE.
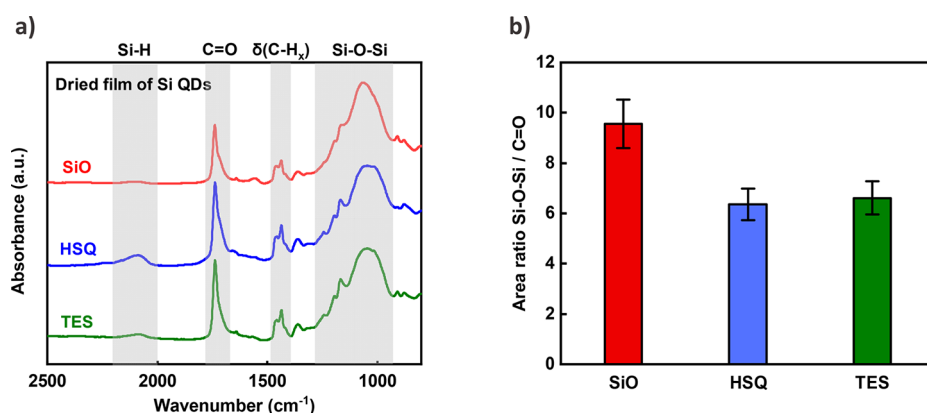
Figure 6. (a) Attenuated total reflectance (ATR) spectra of thin dried films of Si QDs synthesized from SiO (red), HSQ (blue), and TES (green). (b) The ratio of areas under the Si−O−Si and C=O stretching modes obtained from (a).

As shown in Figure 5b, the IQEs of QDs-HSQ and QDs-TES were maintained to be near-unity also after the transition from toluene to the OSTE matrix. Therefore, their PLQY enhancements can only originate from partial conversion of "dark" QDs into "bright" ones, probably by further passivation of dangling bonds in the presence of OSTE.[11,48] For QDs-SiO, the IQE in OSTE still deviates from unity, suggesting persistent nonradiative centers.

To shed light on the origin of these nonradiative processes, we performed attenuated total reflection (FTIR-ATR) measurements on thin dried films of Si QDs. The results are shown in Figure 6a, providing information on the surface properties of these QDs. As can be seen, all of the QDs share the same characteristic peaks. The band at ~2100 cm^{-1} corresponds to the Si−H stretching mode, and the absorption feature at ~1100 cm^{-1} can be assigned to the Si−O−Si stretching vibration. Note that theoretical modeling has proven that Si−O−Si bonds can only exist on the Si QD surface and not inside the nanocrystal.[54] Apart from the coverage of the Si−C bonds (peak unresolved in the spectra) by ligand passivation, there are only Si−O−Si and Si−H bonds on the Si QD surface. Here, there is a consistent one-to-one match between C=O and Si−C bonds, considering the chemical structure of ester ligands. The coverage of Si−H bonds is low, according to the spectra, and can be neglected. Therefore, the ratio between Si−O−Si and C=O (~1750 cm^{-1}) peak areas will reflect relative surface coverage of QDs by the oxide. The ratios of the integrated areas of Si−O−Si and C=O bands are shown in Figure 6b. For QDs-HSQ and QDs-TES, the area ratio is lower than for QDs-SiO, revealing a markedly lower percentage of Si−O−Si coverage on the nanoparticle surface.

The oxide on the surface of Si is a known host for charge trap sites, which was well-documented in Si-based nanoelectronics,[55] and was also explicitly shown for Si QDs in single-dot lifetime measurements.[56] The IQE and, subsequently, the PLQY are expected to be lower in such a system due to the intermittent trapping and detrapping of carriers, resulting in Auger nonradiative recombinations. The excess of oxide phase and intrinsic nonuniformity of SiO makes it challenging to completely eliminate oxide for such QDs even under prolonged HF etching. As a main fundamental result of this study, we, therefore, conclude that the low PLQY values for SiO-derived QDs stem from the precursor intrinsic structure, limiting this material applicability. On the other hand, TES-derived Si QDs can be controlled through the

annealing and etching processes to the quality level matching that of the state-of-the-art precursor HSQ.

In summary, this work introduces a recipe for the synthesis of good-quality, near-infrared emitting Si QDs with ~55% PLQY for QDs/OSTE nanocomposites (~40% ensemble PLQY in toluene) and near-unity IQE by using commercial TES as the precursor. By comparing Si QDs of a similar size (4−5 nm) synthesized from HSQ and SiO by structural, chemical, and optical characterizations, we ascribe the superior optical efficiency of QDs-TES to the uniform QD size distribution and a small quantity of oxide on the surface. A relatively well-defined initial structure of TES and the balance of annealing and etching processes developed here made this result possible. Importantly, having a comparable optical quality with their QDs-HSQ counterparts, the cost of QDs-TES is an order of magnitude lower. For applications requiring a large amount of Si QDs, such as large-area semitransparent PVs, QDs-HSQ are prohibitively expensive, while QDs-SiO are prohibitively optically inefficient. Therefore, commercial TES reported here is a promising pathway for the scalable synthesis of high-quality Si QDs. We believe this method will significantly promote applications requiring high loads of Si QDs, especially in a solid phase, thanks to its low cost and good optical efficiency.

■ ASSOCIATED CONTENT

ⓢ Supporting Information

The Supporting Information is available free of charge at https://pubs.acs.org/doi/10.1021/acs.jpclett.1c02187.

Experimental details; XRD spectra of preannealing powders; low-magnification TEM images of Si QDs; TGA analysis; ATR measurements; synthesis optimization from SiO and TES; reproducibility test; PLQY stability test; PLQY dependency on the excitation wavelength; additional PL decays (PDF)

■ AUTHOR INFORMATION

Corresponding Author

Ilya Sychugov − Department of Applied Physics, KTH - Royal Institute of Technology, Stockholm 10691, Sweden; ⓞ orcid.org/0000-0003-2562-0540; Email: ilyas@kth.se

Authors

Jingjian Zhou − *Department of Applied Physics, KTH - Royal Institute of Technology, Stockholm 10691, Sweden;* ⊙ orcid.org/0000-0002-6623-2491

Jing Huang − *Department of Applied Physics, KTH - Royal Institute of Technology, Stockholm 10691, Sweden*

Huai Chen − *MOE Laboratory of Bioinorganic and Synthetic Chemistry, Lehn Institute of Functional Materials, School of Chemistry, Sun Yat-sen University, Guangzhou 510275 Guangdong, China*

Archana Samanta − *Department of Applied Physics, KTH - Royal Institute of Technology, Stockholm 10691, Sweden;* ⊙ orcid.org/0000-0003-3595-5264

Jan Linnros − *Department of Applied Physics, KTH - Royal Institute of Technology, Stockholm 10691, Sweden*

Zhenyu Yang − *MOE Laboratory of Bioinorganic and Synthetic Chemistry, Lehn Institute of Functional Materials, School of Chemistry, Sun Yat-sen University, Guangzhou 510275 Guangdong, China; Dongguan Institute, Sun Yat-sen University, Dongguan 523808, China;* ⊙ orcid.org/0000-0002-6403-8679

Complete contact information is available at:
https://pubs.acs.org/10.1021/acs.jpclett.1c02187

Notes

The authors declare no competing financial interest.

■ REFERENCES

(1) Erogbogbo, F.; Yong, K.-T.; Roy, I.; Xu, G.; Prasad, P. N.; Swihart, M. T. Biocompatible Luminescent Silicon Quantum Dots for Imaging of Cancer Cells. *ACS Nano* **2008**, *2*, 873−878.

(2) Henderson, E. J.; Shuhendler, A. J.; Prasad, P.; Baumann, V.; Maier-Flaig, F.; Faulkner, D. O.; Lemmer, U.; Wu, X. Y.; Ozin, G. A. Colloidally Stable Silicon Nanocrystals with Near-Infrared Photoluminescence for Biological Fluorescence Imaging. *Small* **2011**, *7*, 2507−2516.

(3) Zhong, Y.; Sun, X.; Wang, S.; Peng, F.; Bao, F.; Su, Y.; Li, Y.; Lee, S.-T.; He, Y. Facile, Large-Quantity Synthesis of Stable, Tunable-Color Silicon Nanoparticles and Their Application for Long-Term Cellular Imaging. *ACS Nano* **2015**, *9*, 5958−5967.

(4) Liu, X.; Zhao, S.; Gu, W.; Zhang, Y.; Qiao, X.; Ni, Z.; Pi, X.; Yang, D. Light-Emitting Diodes Based on Colloidal Silicon Quantum Dots with Octyl and Phenylpropyl Ligands. *ACS Appl. Mater. Interfaces* **2018**, *10*, 5959−5966.

(5) Ghosh, B.; Yamada, H.; Chinnathambi, S.; Özbilgin, İ. N. G.; Shirahata, N. Inverted Device Architecture for Enhanced Performance of Flexible Silicon Quantum Dot Light-Emitting Diode. *J. Phys. Chem. Lett.* **2018**, *9*, 5400−5407.

(6) Huang, J.; Zhou, J.; Haraldsson, T.; Clemments, A.; Fujii, M.; Sugimoto, H.; Xu, B.; Sychugov, I. Triplex Glass Laminates with Silicon Quantum Dots for Luminescent Solar Concentrators. *Solar RRL* **2020**, *4* (9), 2000195.

(7) Meinardi, F.; Ehrenberg, S.; Dhamo, L.; Carulli, F.; Mauri, M.; Bruni, F.; Simonutti, R.; Kortshagen, U.; Brovelli, S. Highly efficient luminescent solar concentrators based on earth-abundant indirect-bandgap silicon quantum dots. *Nat. Photonics* **2017**, *11*, 177−185.

(8) Yu, Y.; Fan, G.; Fermi, A.; Mazzaro, R.; Morandi, V.; Ceroni, P.; Smilgies, D.-M.; Korgel, B. A. Size-Dependent Photoluminescence Efficiency of Silicon Nanocrystal Quantum Dots. *J. Phys. Chem. C* **2017**, *121*, 23240−23248.

(9) Marinins, A.; Yang, Z.; Chen, H.; Linnros, J.; Veinot, J. G. C.; Popov, S.; Sychugov, I. Photostable Polymer/Si Nanocrystal Bulk Hybrids with Tunable Photoluminescence. *ACS Photonics* **2016**, *3*, 1575−1580.

(10) Hessel, C. M.; Reid, D.; Panthani, M. G.; Rasch, M. R.; Goodfellow, B. W.; Wei, J.; Fujii, H.; Akhavan, V.; Korgel, B. A. Synthesis of Ligand-Stabilized Silicon Nanocrystals with Size-Dependent Photoluminescence Spanning Visible to Near-Infrared Wavelengths. *Chem. Mater.* **2012**, *24*, 393−401.

(11) Marinins, A.; Zandi Shafagh, R.; van der Wijngaart, W.; Haraldsson, T.; Linnros, J.; Veinot, J. G. C.; Popov, S.; Sychugov, I. Light-Converting Polymer/Si Nanocrystal Composites with Stable 60−70% Quantum Efficiency and Their Glass Laminates. *ACS Appl. Mater. Interfaces* **2017**, *9*, 30267−30272.

(12) Kanemitsu, Y.; Okamoto, S. Phonon structures and Stokes shift in resonantly excited luminescence of silicon nanocrystals. *Phys. Rev. B: Condens. Matter Mater. Phys.* **1998**, *58*, 9652−9655.

(13) Ghosh, B.; Masuda, Y.; Wakayama, Y.; Imanaka, Y.; Inoue, J.-i.; Hashi, K.; Deguchi, K.; Yamada, H.; Sakka, Y.; Ohki, S.; Shimizu, T.; Shirahata, N. Hybrid White Light Emitting Diode Based on Silicon Nanocrystals. *Adv. Funct. Mater.* **2014**, *24*, 7151−7160.

(14) Yamada, H.; Saitoh, N.; Ghosh, B.; Masuda, Y.; Yoshizawa, N.; Shirahata, N. Improved Brightness and Color Tunability of Solution-Processed Silicon Quantum Dot Light-Emitting Diodes. *J. Phys. Chem. C* **2020**, *124*, 23333−23342.

(15) Mazzaro, R.; Gradone, A.; Angeloni, S.; Morselli, G.; Cozzi, P. G.; Romano, F.; Vomiero, A.; Ceroni, P. Hybrid Silicon Nanocrystals for Color-Neutral and Transparent Luminescent Solar Concentrators. *ACS Photonics* **2019**, *6*, 2303−2311.

(16) Hill, S. K. E.; Connell, R.; Held, J.; Peterson, C.; Francis, L.; Hillmyer, M. A.; Ferry, V. E.; Kortshagen, U. Poly(methyl methacrylate) Films with High Concentrations of Silicon Quantum Dots for Visibly Transparent Luminescent Solar Concentrators. *ACS Appl. Mater. Interfaces* **2020**, *12*, 4572−4578.

(17) Jingjian, Z.; Pevere, F.; Gatty, H. K.; Linnros, J.; Sychugov, I. Wafer-scale fabrication of isolated luminescent silicon quantum dots using standard CMOS technology. *Nanotechnology* **2020**, *31*, 505204.

(18) Sychugov, I.; Nakayama, Y.; Mitsuishi, K. Sub-10 nm crystalline silicon nanostructures by electron beam induced deposition lithography. *Nanotechnology* **2010**, *21*, 285307.

(19) Vendamani, V. S.; Hamad, S.; Saikiran, V.; Pathak, A. P.; Venugopal Rao, S.; Ravi Kanth Kumar, V. V.; Nageswara Rao, S. V. S. Synthesis of ultra-small silicon nanoparticles by femtosecond laser ablation of porous silicon. *J. Mater. Sci.* **2015**, *50*, 1666−1672.

(20) Heath, J. R. A liquid-solution-phase synthesis of crystalline silicon. *Science* **1992**, *258*, 1131−1133.

(21) Mangolini, L.; Kortshagen, U. Plasma-Assisted Synthesis of Silicon Nanocrystal Inks. *Adv. Mater.* **2007**, *19*, 2513−2519.

(22) Jurbergs, D.; Rogojina, E.; Mangolini, L.; Kortshagen, U. Silicon nanocrystals with ensemble quantum yields exceeding 60%. *Appl. Phys. Lett.* **2006**, *88*, 233116.

(23) Pauthe, M.; Bernstein, E.; Dumas, J.; Saviot, L.; Pradel, A.; Ribes, M. Preparation and characterisation of Si nanocrystallites embedded in a silica matrix. *J. Mater. Chem.* **1999**, *9*, 187−191.

(24) Hessel, C. M.; Henderson, E. J.; Veinot, J. G. C. An Investigation of the Formation and Growth of Oxide-Embedded Silicon Nanocrystals in Hydrogen Silsesquioxane-Derived Nanocomposites. *J. Phys. Chem. C* **2007**, *111*, 6956−6961.

(25) Henderson, E. J.; Kelly, J. A.; Veinot, J. G. C. Influence of HSiO1.5 SolGel Polymer Structure and Composition on the Size and Luminescent Properties of Silicon Nanocrystals. *Chem. Mater.* **2009**, *21*, 5426−5434.

(26) Clark, R. J.; Aghajamali, M.; Gonzalez, C. M.; Hadidi, L.; Islam, M. A.; Javadi, M.; Mobarok, M. H.; Purkait, T. K.; Robidillo, C. J. T.; Sinelnikov, R.; Thiessen, A. N.; Washington, J.; Yu, H.; Veinot, J. G. C. From Hydrogen Silsesquioxane to Functionalized Silicon Nanocrystals. *Chem. Mater.* **2017**, *29*, 80−89.

(27) Hessel, C. M.; Henderson, E. J.; Veinot, J. G. C. Hydrogen Silsesquioxane: A Molecular Precursor for Nanocrystalline Si−SiO2 Composites and Freestanding Hydride-Surface-Terminated Silicon Nanoparticles. *Chem. Mater.* **2006**, *18*, 6139−6146.

(28) Islam, M. A.; Mobarok, M. H.; Sinelnikov, R.; Purkait, T. K.; Veinot, J. G. C. Phosphorus Pentachloride Initiated Functionalization of Silicon Nanocrystals. *Langmuir* **2017**, *33*, 8766−8773.

(29) Locritani, M.; Yu, Y.; Bergamini, G.; Baroncini, M.; Molloy, J. K.; Korgel, B. A.; Ceroni, P. Silicon Nanocrystals Functionalized with Pyrene Units: Efficient Light-Harvesting Antennae with Bright Near-Infrared Emission. *J. Phys. Chem. Lett.* **2014**, *5*, 3325−3329.

(30) Sun, W.; Qian, C.; Wang, L.; Wei, M.; Mastronardi, M. L.; Casillas, G.; Breu, J.; Ozin, G. A. Switching-On Quantum Size Effects in Silicon Nanocrystals. *Adv. Mater.* **2015**, *27*, 746−749.

(31) Dorofeev, S. G.; Ischenko, A. A.; Kononov, N. N.; Fetisov, G. V. Effect of annealing temperature on the optical properties of nanosilicon produced from silicon monoxide. *Curr. Appl. Phys.* **2012**, *12*, 718−725.

(32) Kelly, J. A.; Henderson, E. J.; Veinot, J. G. C. Sol−gel precursors for group 14 nanocrystals. *Chem. Commun.* **2009**, *46*, 8704−8718.

(33) Terada, S.; Xin, Y.; Saitow, K.-i. Cost-Effective Synthesis of Silicon Quantum Dots. *Chem. Mater.* **2020**, *32*, 8382−8392.

(34) Mastronardi, M. L.; Maier-Flaig, F.; Faulkner, D.; Henderson, E. J.; Kübel, C.; Lemmer, U.; Ozin, G. A. Size-Dependent Absolute Quantum Yields for Size-Separated Colloidally-Stable Silicon Nanocrystals. *Nano Lett.* **2012**, *12*, 337−342.

(35) Chinnathambi, S.; Hanagata, N.; Yamazaki, T.; Shirahata, N. Nano-Bio Interaction between Blood Plasma Proteins and Water-Soluble Silicon Quantum Dots with Enabled Cellular Uptake and Minimal Cytotoxicity. *Nanomaterials* **2020**, *10*, 2250.

(36) Xie, Z.; Henderson, E. J.; Dag, Ö.; Wang, W.; Lofgreen, J. E.; Kübel, C.; Scherer, T.; Brodersen, P. M.; Gu, Z.-Z.; Ozin, G. A. Periodic Mesoporous Hydridosilica − Synthesis of an "Impossible" Material and Its Thermal Transformation into Brightly Photoluminescent Periodic Mesoporous Nanocrystal Silicon-Silica Composite. *J. Am. Chem. Soc.* **2011**, *133*, 5094−5102.

(37) Das, G.; Ferraioli, L.; Bettotti, P.; De Angelis, F.; Mariotto, G.; Pavesi, L.; Di Fabrizio, E.; Soraru, G. D. Si-nanocrystals/SiO2 thin films obtained by pyrolysis of sol−gel precursors. *Thin Solid Films* **2008**, *516*, 6804−6807.

(38) Ghosh, B.; Takeguchi, M.; Nakamura, J.; Nemoto, Y.; Hamaoka, T.; Chandra, S.; Shirahata, N. Origin of the Photoluminescence Quantum Yields Enhanced by Alkane-Termination of Freestanding Silicon Nanocrystals: Temperature-Dependence of Optical Properties. *Sci. Rep.* **2016**, *6*, 36951.

(39) Chandra, S.; Ghosh, B.; Beaune, G.; Nagarajan, U.; Yasui, T.; Nakamura, J.; Tsuruoka, T.; Baba, Y.; Shirahata, N.; Winnik, F. M. Functional double-shelled silicon nanocrystals for two-photon fluorescence cell imaging: spectral evolution and tuning. *Nanoscale* **2016**, *8*, 9009−9019.

(40) Baney, R. H.; Itoh, M.; Sakakibara, A.; Suzuki, T. *Chem. Rev.* **1995**, *95*, 1409−1430.

(41) Hirata, A.; Kohara, S.; Asada, T.; Arao, M.; Yogi, C.; Imai, H.; Tan, Y.; Fujita, T.; Chen, M. Atomic-scale disproportionation in amorphous silicon monoxide. *Nat. Commun.* **2016**, *7*, 11591.

(42) Liu, S.-M.; Yang; Sato, S.; Kimura, K. Enhanced Photoluminescence from Si Nano-organosols by Functionalization with Alkenes and Their Size Evolution. *Chem. Mater.* **2006**, *18*, 637−642.

(43) Kapaklis, V.; Politis, C.; Poulopoulos, P.; Schweiss, P. Photoluminescence from silicon nanoparticles prepared from bulk amorphous silicon monoxide by the disproportionation reaction. *Appl. Phys. Lett.* **2005**, *87*, 123114.

(44) Canham, L. Introductory lecture: origins and applications of efficient visible photoluminescence from silicon-based nanostructures. *Faraday Discuss.* **2020**, *222*, 10.

(45) Sun, W.; Qian, C.; Cui, X. S.; Wang, L.; Wei, M.; Casillas, G.; Helmy, A. S.; Ozin, G. A. Silicon monoxide − a convenient precursor for large scale synthesis of near infrared emitting monodisperse silicon nanocrystals. *Nanoscale* **2016**, *8*, 3678−3684.

(46) Luo, J.-W.; Stradins, P.; Zunger, A. Matrix-embedded silicon quantum dots for photovoltaic applications: a theoretical study of critical factors. *Energy Environ. Sci.* **2011**, *4*, 2546−2557.

(47) Li, Y.-S.; Ba, A. Spectroscopic studies of triethoxysilane sol−gel and coating process. *Spectrochim. Acta, Part A* **2008**, *70*, 1013−1019.

(48) Sefannaser, M.; Thomas, S. A.; Anderson, K. J.; Petersen, R. J.; Brown, S. L.; Boudjouk, P. R.; Pringle, T. A.; Hobbie, E. K. Radiative Relaxation in Luminescent Silicon Nanocrystal Thiol-Ene Composites. *J. Phys. Chem. C* **2021**, *125*, 5824.

(49) Sychugov, I. Analytical description of a luminescent solar concentrator. *Optica* **2019**, *6*, 1046−1049.

(50) Sychugov, I.; Fucikova, A.; Pevere, F.; Yang, Z.; Veinot, J. G. C.; Linnros, J. Ultranarrow Luminescence Linewidth of Silicon Nanocrystals and Influence of Matrix. *ACS Photonics* **2014**, *1*, 998−1005.

(51) Sangghaleh, F.; Sychugov, I.; Yang, Z.; Veinot, J. G. C.; Linnros, J. Near-Unity Internal Quantum Efficiency of Luminescent Silicon Nanocrystals with Ligand Passivation. *ACS Nano* **2015**, *9*, 7097−7104.

(52) Greben, M.; Khoroshyy, P.; Liu, X.; Pi, X.; Valenta, J. Fully radiative relaxation of silicon nanocrystals in colloidal ensemble revealed by advanced treatment of decay kinetics. *J. Appl. Phys.* **2017**, *122*, 034304.

(53) Kůsová, K.; Popelář, T. On the importance of onset times and multiple-wavelength analysis of photoluminescence decays. *J. Appl. Phys.* **2019**, *125*, 193103.

(54) Eyre, R. J.; Goss, J. P.; Briddon, P. R. Density functional study of oxygen migration processes for silicon quantum dots. *Phys. Rev. B: Condens. Matter Mater. Phys.* **2007**, *76*, 245325.

(55) Zhuge, J.; Wang, R.; Huang, R.; Tian, Y.; Zhang, L.; Kim, D.; Park, D.; Wang, Y. Investigation of Low-Frequency Noise in Silicon Nanowire MOSFETs. *IEEE Electron Device Lett.* **2009**, *30*, 57−60.

(56) Pevere, F.; Sangghaleh, F.; Bruhn, B.; Sychugov, I.; Linnros, J. Rapid Trapping as the Origin of Nonradiative Recombination in Semiconductor Nanocrystals. *ACS Photonics* **2018**, *5*, 2990−2996.

Supporting Information

Low-cost Synthesis of Silicon Quantum Dots with Near-Unity Internal Quantum Efficiency

Jingjian Zhou[1], Jing Huang[1], Huai Chen[2], Archana Samanta[1], Jan Linnros[1], Zhenyu Yang[2,3], Ilya Sychugov[1,*]

[1]Department of Applied Physics, KTH - Royal Institute of Technology, Stockholm 10691, Sweden
[2]MOE Laboratory of Bioinorganic and Synthetic Chemistry, Lehn Institute of Functional Materials, School of Chemistry, Sun Yat-Sen University, Guangzhou 510275, Guangdong, China
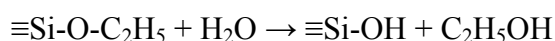[3]Dongguan Institute, Sun Yat-sen University, Dongguan, 523808, China

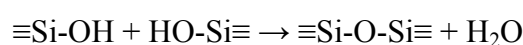*Email: ilyas@kth.se

<u>Section S1. Experimental Details</u>

Preparation of TES-derived xerogels
First, in a 100 mL Schlenk flask 10 mL of 90 mmol/L HNO_3 and 10 mL of ethanol were mixed with magneton stirring in an argon atmosphere. Then, 55 mmol (approximately 10 mL) of 95% triethoxysilane (TES) (Sigma-Aldrich, 95%) was slowly added into the flask drop by drop in an ice bath. A transparent gel-like polymer was formed and then aged for 72 hours. Products were purified with ethanol to remove unreacted TES and then transferred to vacuum to remove residual ethanol and water at room temperature for 24 hours. After drying, xerogels were prepared.

Hydrolysis
$$\equiv Si\text{-}O\text{-}C_2H_5 + H_2O \rightarrow \equiv Si\text{-}OH + C_2H_5OH$$
Condensation
$$\equiv Si\text{-}OH + HO\text{-}Si \equiv \rightarrow \equiv Si\text{-}O\text{-}Si \equiv + H_2O$$

Si QDs Synthesis
The synthesis of Si QDs follows a variation of published methods and parameters of annealing differs from one precursor to another.
For TES method, the TES-derived xerogels were annealed at 600°C for 1h to remove residual carbon and solvent and then annealed at 950°C for 1h in a 95% Argon / 5% H_2 atmosphere. To facilitate subsequent etching process, 100 mg of the annealed brown powder together with 3 mL of ethanol was grinded with a mortar and pestle and then transferred into a polypropylene centrifuge tube. 10 mL of 50% aqueous hydrofluoric acid (HF) was then carefully added to the mixture under magnetic stirring. *Caution: HF solution is extremely dangerous. One has to receive professional safety training and specific safety equipment is necessary in operation.* In 1h, the colour turned from dark brown at the beginning to light brown, and no more turbidness can be observed in the solution. Subsequently, 20 mL of toluene was used to extract hydride Si QDs from the aqueous solution for twice (10 mL each), followed by centrifuged at 10000 rpm for 10 min. The precipitate was collected for hydrosilylation.
To obtain ligand-terminated Si QDs, the precipitate was mixed with 2.5 mL of methyl 10-undercenoate (Sigma-Aldrich, 96%), under ultrasonic for 5 min to obtain a homogeneous mixture. The suspension was then transferred to a flask and connected to an argon-filled Schlenk line to prevent from oxygen. The surface passivation reaction was kept at 150°C for 19 h. Si QDs can be extracted from ester solution by adding 4 times volume of antisolvent, which is hexane here, followed by centrifuge at 10000 rpm for 10 min. The precipitate was collected and redispersed in toluene.
For HSQ method, commercial hydrogen silsesquioxane (HSQ) from Applied Quantum Materials Inc. (Canada) was annealed at 1200°C for 1h in a 95% Argon / 5% H_2 atmosphere. 100 mg of the fine Si QDs/SiO_2 powder was mixed with 3 ml of ethanol and 3 ml of DI water subsequently in a polypropylene centrifuge tube under magnetic stirring. A 50% aqueous hydrofluoric acid (HF) solution (3 ml) was then slowly added to the mixture under stirring. The suspension turned yellow after stirring for 1 h, indicating that the Si QDs were released from SiO_2 matrix. The resulted hydride-terminated nanoparticles were collected by extractions with 10 ml of toluene for three times, followed by centrifuged at 10000 rpm for 10 min. The precipitate was then collected for surface passivation. For surface passivation, the fresh hydride

Si QDs were mixed with 3 mL of methyl 10-undecenoate and the mixture was sonicated for 5 min to get homogeneous wetting. Then the suspension was loaded in a flask and transferred to an argon-charged Schlenk line. The reaction mixture was kept at 150°C for 19 h under Ar atmosphere, and the brown suspension changed to a clear orange/brown solution, which was kept directly for further application.

For SiO method, silicon monoxide (SiO) from Sigma-Aldrich was annealed at 920°C for 1h in a 95% Argon / 5% H_2 atmosphere. 25 mg of the fine Si QDs/SiO$_2$ powder was mixed with 3 ml of ethanol subsequently in a polypropylene centrifuge tube under magnetic stirring. A 50% aqueous hydrofluoric acid (HF) solution (10 ml) was then slowly added to the mixture under stirring. The suspension turned yellow after stirring for 5 h, indicating that the Si QDs were released from SiO$_2$ matrix. The resulted hydride-terminated nanoparticles were collected by extractions with 10 ml of toluene for three times, followed by centrifuged at 10000 rpm for 10 min. The precipitate was then collected for surface passivation. For surface passivation, the fresh hydride Si QDs were mixed with 2.5 mL of methyl 10-undecenoate and the mixture was sonicated for 5 min to get homogeneous wetting. Then the suspension was loaded in a flask and transferred to an argon-charged Schlenk line. The reaction mixture was kept at 150°C for 19 h under Ar atmosphere, and the brown suspension changed to a clear orange/brown solution, which was kept directly for further application.

Fabrication of Si QDs/OSTE nanocomposite

Pentaerythritol tetrakis (3-mercaptobutylate) was used as thiol monomer and triallyl-1,3,5-triazine-2,4,6 (1H,3H,5H)-trione as allyl monomer. Photo-initiator is 1-Hydroxycyclohexyl phenyl ketone (Irgacure-184). All of them were from Mercene Labs AB, Sweden. First, in a glass vial ~2 mg of Si QDs was dispersed in 0.96 g of allyl monomer under ultrasonication. Then, 3.11 g thiol monomer and 0.04 g photo-initiator were added to the orange solution and mixed thoroughly. The sticky solution was put in an evacuated desiccator to remove the air bubbles trapped inside. At last, the homogeneous solution was cured by 360 nm UV light for 30s to trigger thiol-ene polymerization reaction and stored overnight to complete the polymerization.

Structural and standard absorption measurements

To prepare TEM samples, Si QDs in toluene solutions were drop-casted dropped on a ~15 nm thick amorphous silicon nitride (SiN) support films and dried. Transmission electron microscope (TEM) images of Si QDs were obtained from a JEM-2100F TEM operated at 200 kV. Attenuated total reflection (ATR) spectra were obtained using a Spectrum 100 Fourier transform infrared (FTIR) spectrometer (PerkinElmer, USA) equipped with a Golden Gate diamond ATR (Gaseby Specac Ltd, UK). The spectra were recorded at room temperature with a resolution of 4 cm^{-1} from 4000 to 400 cm^{-1}. Si QDs in toluene solutions were drop-casted dropped on a glass slide and dried until a film of QDs formed. UV-vis absorption spectra were collected on Lambda 750 UV-vis spectrophotometer for Si QDs in toluene solution.

X-ray diffraction (XRD) measurements

XRD patterns were collected with a Rigaku Smart Lab diffractometer (Bragg-Brentano geometry, Cu Kα1 radiation, λ = 1.54056 Å). The spectra were scanned between 2θ ranges of 10–80° with an integration of 350 min.

Thermogravimetric analysis (TGA)

Thermogravimetric analysis (TGA) was conducted on a, Mettler Toledo (TGA/DSC1, Switzerland) instrument. Samples (~10 mg) were placed in alumina pans and heated from 25 to 900 °C with a heating rate of 10 °C min^{-1} in a N_2 flow of 50 mL/min.

Optical measurements
Photoluminescence quantum yield (PLQY)

A home-built integrating sphere setup was utilized to measure absolute PLQY of Si QDs in toluene solution and Si QDs in OSTE matrix. A laser-driven xenon plasma white-light source (Energetic, EQ-99) was used as the excitation source, coupled with a tunable wavelength-selected monochromator (SP2150i, Princeton Instruments). In a 6-inch-diameter integrating sphere (Labsphere), photoluminescence of the excited sample was collected at the bottom port, which was connected through optical fibers to a spectrometer and a Peltier element-cooled CCD camera (-75°C, Princeton Instruments) for signal acquisitions. By using the same monochromatic light source calibrated with an optical power meter (Newport), the system response curve was evaluated for the same spectrometer grating central wavelengths as in measurements. Each spectrum of the sample was calibrated with the system response and then subtracted from the calibrated reference spectrum (without QDs). Through integrations the calculated absorbed and emitted photon numbers per unit time can be obtained. The absolute PLQY is defined as the ratio of absorbed and emitted photon numbers. Another commercial and research-grade QY setups was employed to test the accuracy of this home-built apparatus, as well as benchmarking on organic dyes, such as Rh6G, confirmed the relative error ~ 10%. Unless otherwise specified the excitation at 440 nm was employed in this work.

Micro-photoluminescence (μ-PL) setup and Spectrally Resolved Decay

The excitation beam (a λ_{exc} = 405 nm diode laser) was directed to the sample from outside with a power density of 15W cm^{-2} in a dark-field configuration. The PL emission from the sample was collected by an inverted optical microscope (Zeiss Axio Observer Z1) with a 100x objective lens (Nikon, NA = 0.73 and field-of-view 150 μm) or a 10x objective lens (Zeiss, NA = 0.25 and field-of-view 1.3 mm). It was filtered from the excitation light using a series of 442 and 561 nm long-pass filters (Semrock) and then captured by a spectrometer (Andor Shamrock 500) connected to the left port of the microscope, with a tunable slit at the input and two different gratings of spectral resolution 0.9 and 0.08 nm. A thermoelectrically-cooled EMCCD camera (Andor iXon3 888) was attached to the spectrometer for imaging and an avalanche photodiode (Becker & Hickl, DPC-230) was attached to collect the emitted photons in time-resolved mode. For spectrally resolved decay measurements, a pulsed laser beam was applied with pulse width between 100-500 μs and frequency between 0.3-2 kHz, depending on the selected detection energy. An avalanche photodiode (Becker & Hickl, DPC-230) was used after a spectrometer (Andor Shamrock 500) in order to detect the emitted PL photons collected by a 10x objective lens (NA ≈ 0.25). Through the introduced numerical method in the literature, the spectrally resolved decays of Si NCs were mathematically converted to size-selected decays, excluding the homogenous linewidth broadening in spectrally resolved measurements. Given the E_0 (the ensemble PL center wavelength), ω_{ens} (the width of the ensemble distribution), ω_{hom} (a

homogenous peak width, ~200 meV), and $\tau_{0m}(\varepsilon)$ (the measured lifetime for a certain detection energy ε), by solving an inverse problem the intrinsic lifetime $\tau_{0i}(\varepsilon)$ can be extracted considering the effect of homogenous broadening on the measured lifetime. The total recombination rate is the inverse of the intrinsic lifetime for a certain detection energy. The steps of IQE analysis are listed below:

1. Acquire the PL emission spectrum of the ensemble sample and extract the ensemble PL center wavelength E_0 and the full width at half maximum of the ensemble distribution ω_{ens}. Assume the homogenous peak width ω_{hom} at room temperature is around 200 meV.

2. Measure the spectrally-resolved PL decays of the ensemble sample at a series of detection energies ε at room temperature.

3. Extract the measured lifetime for a certain detection energy $\tau_{0m}(\varepsilon)$ by fitting PL decays with a stretched exponential decay function $I = I_0\exp\left(-(t/\tau)^\beta\right)$, where τ is the lifetime and β is the dispersion factor. The method is applicable for samples exhibiting spectrally resolved decays with a high β values (>0.85).

4. Take out the intrinsic lifetime from the measured lifetime by numerically excluding the homogenous linewidth broadening. Below are main steps:

(1) Assume the initial values of the intrinsic lifetime at four selected detection energies.

(2) Construct four decay curves at selected detection energies using the mathematical function introduced in the REF 51, where the effect of the homogeneous linewidth broadening on the intrinsic lifetime is numerically considered.

(3) Compare the simulated decay parameters with the corresponding measured ones.

(4) Modify the assumed values of the intrinsic lifetime and repeat the above process in several iterations until the simulated parameters coincide well with the measured ones.

5. Plot the obtained intrinsic total recombination rates as a function of the detection energy. The total recombination rate is the inverse of the intrinsic lifetime for a certain detection energy.

6. Compare with a 100% IQE reference sample to establish possible deviations.
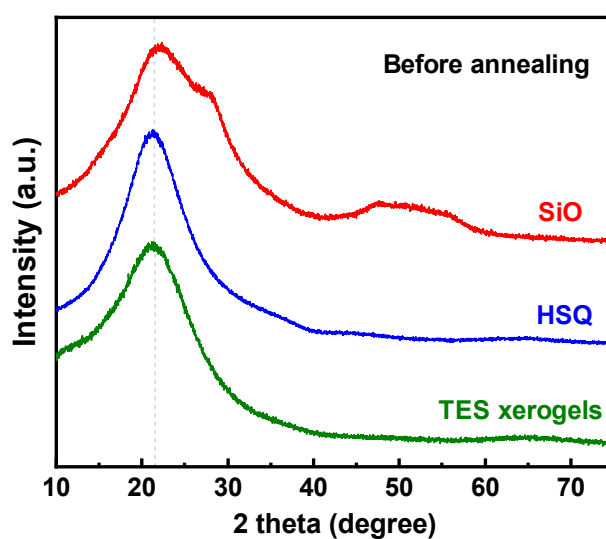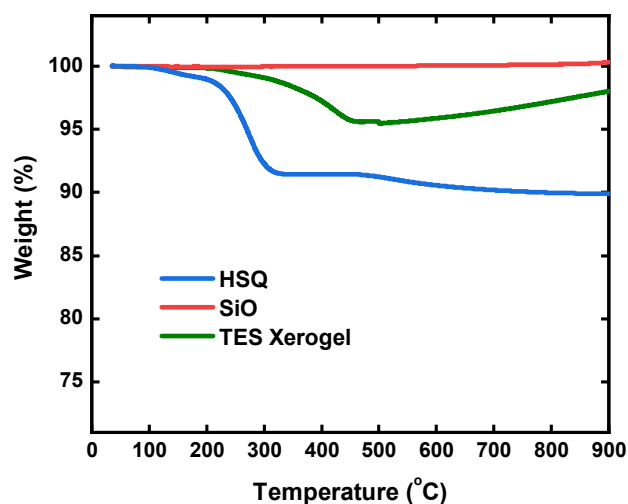
**Figure S1.** X-ray diffraction (XRD) spectra of three preannealed powders.
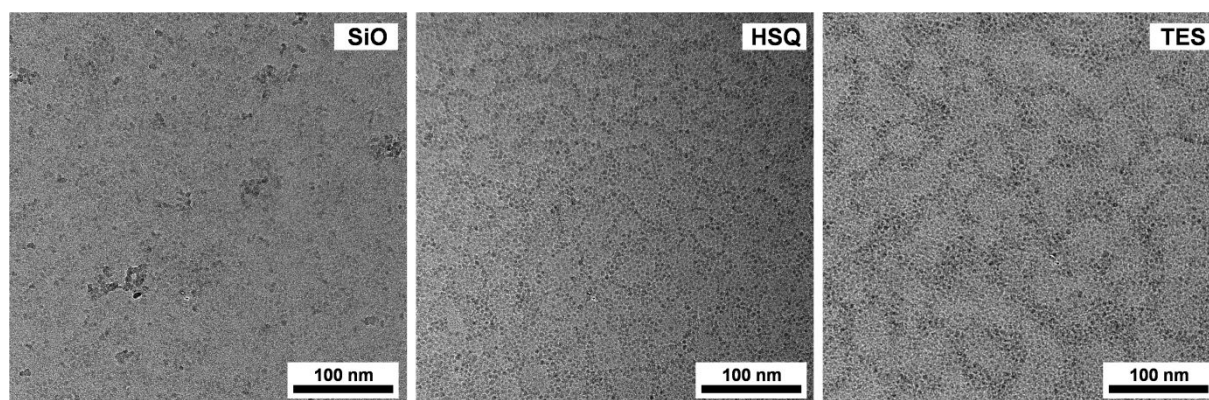
Figure S2. low-magnification TEM images of Si QDs.

The chaos of agglomerations and large particles ($>$6 nm) can be clearly observed in the QDs-SiO sample, while not in the other two samples. These particles of poor qualities would lower the ensemble PLQY of the QDs-SiO sample.

Figure S3. Thermalgravimetric analysis (TGA) curves of HSQ (blue), SiO (red) and TES-derived xerogel (green); heating rate 10°C/min from 30 to 900°C under 100% N_2 atmosphere.

From the TGA curves, SiO barely lose mass during heating from 30 to 900°C under 100% N_2 atmosphere. For HSQ and TES-derived xerogel, they both lose some mass from 130 to 220°C due to moisture, trace solvent and adsorbed CO_2 remained from the beginning. For TES-derived xerogels from 220 to 450°C it is the main loss of heating, which is attributed to the incomplete hydrolysis (residual TES) and incomplete condensation (residual silanol). For the mass loss of HSQ from 220 to 350°C, the cage network distribution and associate loss of SiH_4 are the reason. And for the additional loss from 450 to 700 °C, it can be attributed to the decomposition of SiH_4 to silicon clusters and hydrogen. The latter would be taken away by the flowing atmosphere gas.
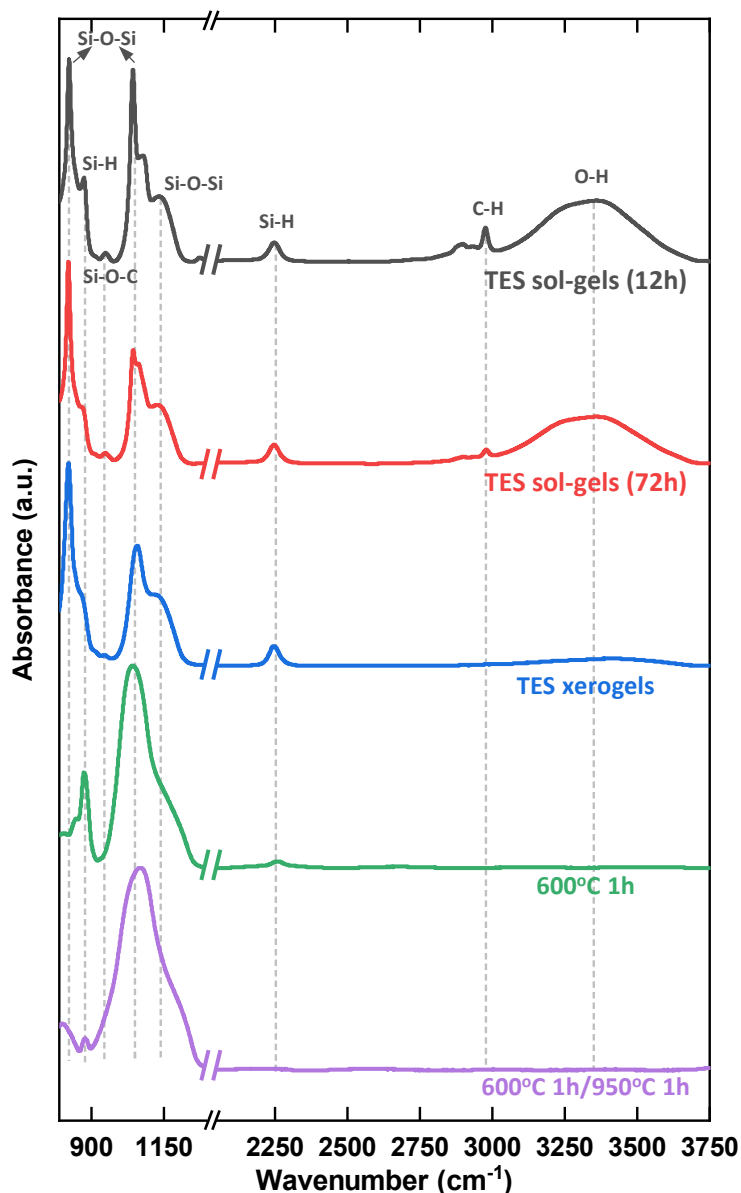
Figure S4. Attenuated total reflectance (ATR) spectra of TES sol-gels after aging for 12h (black), 72h (red), TES xerogels (blue), xerogels annealed at 600°C for 1h (green) and xerogels annealed at 600°C for 1h and 950°C for 1h (purple).

The ATR spectra of TES sol-gels after aging for 12h (black) and 72h (red) were both dominated with ethanol bands, where the broad band at 3400 cm^{-1} (rightmost) refers to the O-H stretching (from incomplete condensation or residual solvent) and the small peak located at 2985 cm^{-1} refers to the C-H stretching. In addition, the Si-O-Si network vibration is responsible for the intense peak at 830 cm^{-1} (leftmost) and the strong band at around 1100 cm^{-1}. The hump at 870 cm^{-1} and the peak at 2250 cm^{-1} both characterize the Si-H bending in the TES sol-gels. At 955 cm^{-1}, the appearance of Si-O-C stretching mode shows that the hydrolysis was incomplete. After drying for 24h under vacuum, the C-H stretching peak vanished from the spectrum (blue) of the TES xerogels (below the detection threshold) while the small hump from Si-O-C still

existed, which either originated from the residual TES or the ethoxy groups bonded to the polymer network (as illustrated in Figure 1). Additionally, the presence of O-H stretching band indicated that the condensation was still incomplete. After annealed at 600°C for 1h, no carbon or ethanol-related bands (below the detection threshold) existed in the spectrum (green), signifying the upgraded main product purity for the subsequent high-temperature annealing. Followed by 950°C annealing for 1h, the Si-H bending band almost disappeared from the spectrum (purple), which was fully consumed as the Si QDs formed. To summarize, the combination of 72h aging, 24h vacuum drying and the preannealing at 600°C for 1h ensured the purity of the polymer product, which should be beneficial to the subsequent formation of Si QDs.

Section S3. Synthesis optimization from SiO

Table S1. Optimizations of QD synthesis from SiO.

Precursor	T	t	Etching time	Amount of HF (mL)	Mass of annealed powder	PL Peak position	PLQY
SiO	1000 °C	20 min	3 h			840 nm	10±1%
	920 °C	30 min	3 h	10 mL	25 mg	850 nm	10±1%
	920 °C	1 h	3 h			870 nm	10±1%
			6 h			820 nm	15±2%

A balance of annealing and etching for synthesis of QDs-SiO was investigated. However, the PLQY of QDs-SiO in toluene was all around 10%, up to 15%. The sample used for comparisons was under conditions of 920 °C annealing for 1h and etching for 6 h.

Section S4. synthesis optimization from TES

Table S2. PL peak position as an effect of t_1.

Precursor	T_1	t_1	T_2	t_2	Etching time	PL Peak position
TES	600 ℃	0 h	950℃	1 h	0.5 h	960 nm
		1 h				885 nm

Without effective decarbonization, the energy barrier for diffusion of Si atoms would be lower, thereby larger particles being formed.

Table S3. PL peak position as an effect of amount of HF per unit mass of annealed powder.

Precursor	T_1	t_1	T_2	t_2	Etching time	Amount of HF (mL)	Mass of annealed powder	PL Peak position	PLQY
TES	600 ℃	1 h	950℃	1 h	1 h	10 mL	50 mg	850 nm	40±4%
							100 mg	850 nm	40±4%
							150 mg	850 nm	40±4%

The relative amount of HF for unit mass of annealed powder has almost no effect on the PL peak position of emission. This implies that the amount of HF used here is far more enough, at least for 150 mg annealed powders.

Table S4. PL peak position as an effect of etching time.

Precursor	T_1	t_1	T_2	t_2	Etching time	Amount of HF (mL)	Mass of annealed powder	PL Peak position	PLQY
TES	600 ℃	1 h	1000℃	1 h	1 h	10 mL	50 mg	920 nm	/
					2 h			860 nm	40±4%
					6 h			800 nm	30±3%

The PL peak position is blue-shifted with a longer HF etching time, implying a size reduction of Si QDs.

Table S5. Annealing and etching conditions of green squares in Figure 3.

No.	Annealing	Etching time	PL Peak position	PLQY in Toluene
1	600℃ for 1h and 900℃ for 1h	0.5h	825 nm	20±2%
2	600℃ for 1h and 925℃ for 1h	0.5h	850 nm	35±4%
3	600℃ for 1h and 950℃ for 1h	0.5h	885 nm	35±4%
4	600℃ for 1h and 1000℃ for 1h	1h	920 nm	/
5	600℃ for 1h and 1100℃ for 1h	2 h	985 nm	/

Table S6. Annealing and etching conditions of red triangles in Figure 3.

No.	Annealing	Etching time	PL Peak position	PLQY in Toluene
1	600°C for 1h and 950°C for 1h	1h	850 nm	40±4%
2	600°C for 1h and 1000°C for 1h	2h	860 nm	40±4%

Table S7. QD mass yield as an effect of etching time.

No.	Annealing	Etching time	PL Peak center wavelength	PLQY in Toluene	PL emission ratio	Mass yield of etching[a]
1	925°C for 1h	0.5h	~850 nm	~35%	~4.0	~6.5%
2	950°C for 1h	1h	~850 nm	~40%	~2.5	~4%
3	1000°C for 1h	2h	~860 nm	~40%	1	~1.5%

[a]Note that, to calculate mass yields, the relative mass of Si QDs is estimated from PL emission, not from weight. According to the vendor, the mass yield of Si QDs from annealed HSQ is ~10% (this value, of course, can vary slightly from different ligands used for QDs surface passivation), used here as a reference roughly corresponding the PL emission to the mass of Si QDs.

With longer etching time, the mass yield of Si QDs drops. Some Si QDs can be fully etched off with a certain time of etching.

Table S8. PL peak position as an effect of t_2.

Precursor	T_1	t_1	T_2	t_2	Etching time	PL Peak position	PLQY in Toluene
TES	600 °C	1 h	1000°C	1 h	2 h	860 nm	40±4%
				5 h		915 nm	40±10%*

*The measurements error is larger because of the low detector sensitivity above 900 nm.

Prolonging the t_2 would contribute to large size of Si QDs, but not as effective as increasing the annealing temperature. Moreover, the PLQY of Si QDs would not further increase with extended t_2, which implies that 1h annealing at high temperature (T_2) is sufficient enough for forming high-quality Si QDs.

Estimation of QD mass yield (QDs-TES as an example)

From 10mL TES (0.89g/mL), ~2.5 g xerogels can be prepared. The mass loss from annealing is ~8%. So the mass yield from TES to annealed powders is ~25%. As for etching, the mass yield of ething is ~4%. This means ~90 mg Si QDs can be prepared from 2.2 g of annealed powders. In total, the mass yield of QDs-TES from precursor is ~1%.

Section S5. Reproducibilty test, stability test, PLQY dependency on the excitation wavelength and PL decays.

Table S9. Reproducibility of different batches.

Batch	PL Peak Position	PLQY in toluene
one	850 nm	43±4%
second	860 nm	42±4%
third	850 nm	40±4%
fourth	900 nm	32±3%
fifth	855 nm	40±4%
sixth	870 nm	41±4%
seventh	850 nm	39±4%

This QD-TES recipe shows good reproducibility (except the fourth batch with shifted PL peak position).
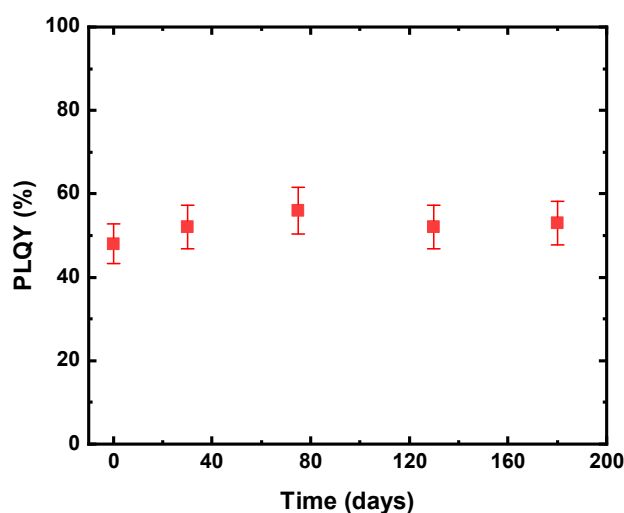

Figure S5. PLQY Stability of Si QDs-TES/OSTE nanocomposite.

The PLQY of QDs-TES/OSTE nanocomposite can be stable for at least 180 days of storage under ambient conditions. The slight variations are attributed to the measurement errors.
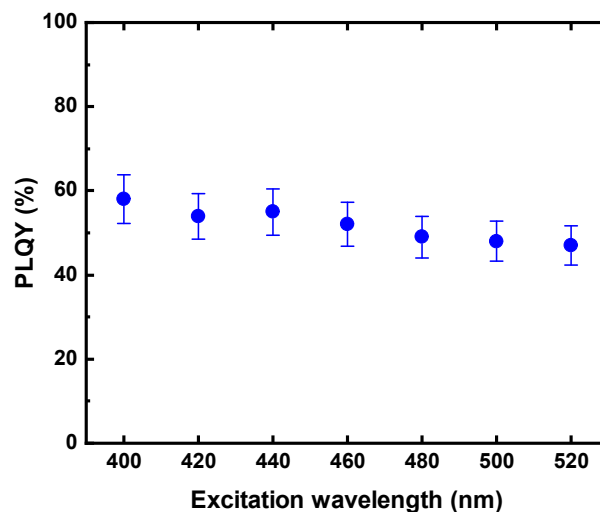
Figure S6. The PLQY dependence on the excitation wavelength of QDs-TES/OSTE nanocomposite.

The PLQY of QDs-TES/OSTE nanocomposite is essentially independent of the excitation wavelength from 400 nm to 520 nm.
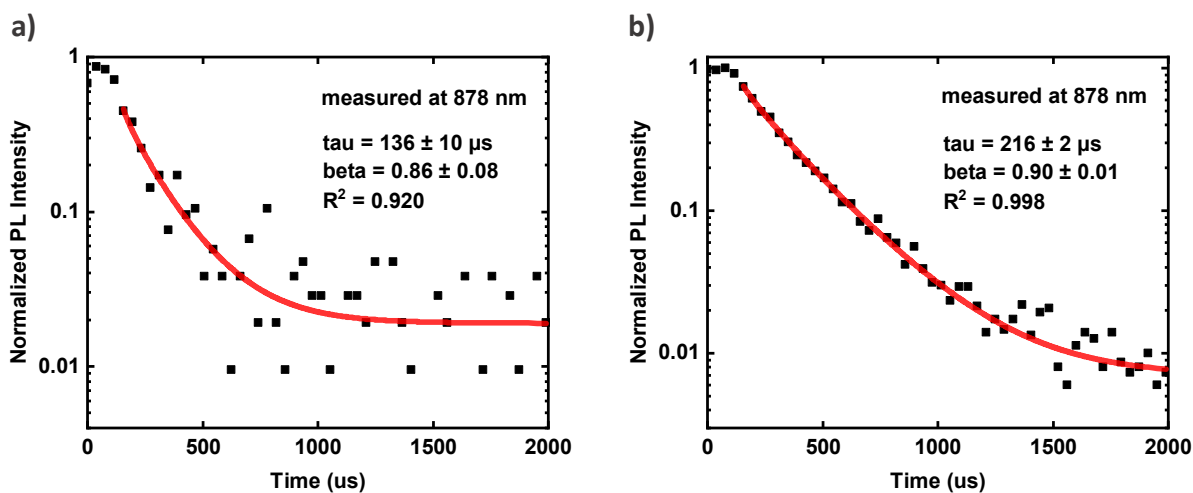
Figure S7. Spectrally resolved PL decays of a) QDs-SiO and b) QDs-HSQ detected at 878 nm and their stretched exponential fits. The signal of QDs-SiO is noisy because of its low quantum yield, corresponding to low PL intensity detected.

Obviously, the PL lifetime of QDs-SiO measured at 878 nm is much shorter than those of QDs-HSQ and QDs-TES and its dispersion factor "beta" is further away from unity.